JACS
JOURNAL OF THE AMERICAN CHEMICAL SOCIETY

ARTICLE

pubs.acs.org/JACS

A New Family of 1D Exchange Biased Heterometal Single-Molecule Magnets: Observation of Pronounced Quantum Tunneling Steps in the Hysteresis Loops of Quasi-Linear $\{Mn_2Ni_3\}$ Clusters

Animesh Das,† Klaus Gieb,‡ Yulia Krupskaya,§ Serhiy Demeshko,† Sebastian Dechert,† Rüdiger Klingeler,§ Vladislav Kataev,*,§ Bernd Büchner,§ Paul Müller,*,‡ and Franc Meyer*,†

†Institut für Inorganic Chemistry, Georg-August-University Göttingen, Tammannstrasse 4, D-37077 Göttingen, Germany
‡Department of Physics, Universität Erlangen-Nürnberg, Erwin-Rommel-Strasse 1, D-91058 Erlangen, Germany
§Leibniz-Institute for Solid State and Materials Research IFW Dresden, P.O. Box 270116, D-01171 Dresden, Germany

Supporting Information

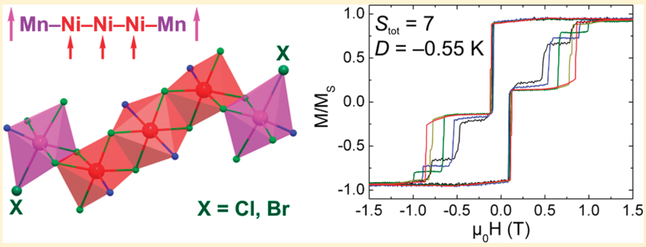

ABSTRACT: First members of a new family of heterometallic Mn/Ni complexes $[Mn_2Ni_3X_2L_4(LH)_2(H_2O)_2]$ (X = Cl: **1**; X = Br: **2**) with the new ligand 2-{3-(2-hydroxyphenyl)-1*H*-pyrazol-1-yl}ethanol (H_2L) have been synthesized, and single crystals obtained from CH_2Cl_2 solutions have been characterized crystallographically. The molecular structures feature a quasi-linear $Mn^{III}-Ni^{II}-Ni^{II}-Ni^{II}-Mn^{III}$ core with six-coordinate metal ions, where elongated axes of all the distorted octahedral coordination polyhedra are aligned parallel and are fixed with respect to each other by intramolecular hydrogen bonds. **1** and **2** exhibit quite strong ferromagnetic exchange interactions throughout ($J_{Mn-Ni} \approx 40$ K (**1**) or 42 K (**2**); $J_{Ni-Ni} \approx 22$ K (**1**) or 18 K (**2**)) that lead to an $S_{tot} = 7$ ground state, and a sizable uniaxial magnetoanisotropy with D_{mol} values −0.55 K (**1**) and −0.45 K (**2**). These values are directly derived also from frequency- and temperature-dependent high-field EPR spectra. Slow relaxation of the magnetization at low temperatures and single-molecule magnet (SMM) behavior are evident from frequency-dependent peaks in the out-of-phase ac susceptibilities and magnetization versus dc field measurements, with significant energy barriers to spin reversal $U_{eff} = 27$ K (**1**) and 22 K (**2**). Pronounced quantum tunnelling steps are observed in the hysteresis loops of the temperature- and scan rate-dependent magnetization data, but with the first relaxation step shifted above (**1**) or below (**2**) the zero crossing of the magnetic field, despite the very similar molecular structures. The different behavior of **1** and **2** is interpreted in terms of antiferromagnetic (**1**) or ferromagnetic (**2**) intermolecular interactions, which are discussed in view of the subtle differences of intermolecular contacts within the crystal lattice.

INTRODUCTION

Certain high-spin molecules with an easy axis (Ising-type) magnetic anisotropy show bistability due to slow magnetic relaxation of the spin reorientation along the magnetic anisotropy axis. These molecules, called single molecule magnets (SMM), have a double minimum potential with a significant barrier for the reversal of the magnetic moment, which is why at very low temperature the spin flips via quantum processes only. This results in a hysteresis of the magnetization that is of purely molecular origin.[1] SMMs are attracting particular interest in chemistry, physics, and materials sciences because they show novel phenomena at the classical/quantum interface, and because they are considered as promising nanoscale objects for, inter alia, future high-density memory storage devices and quantum computing technologies.[2]

Since the discovery in 1993 of the first SMM, the dodecanuclear mixed-valent manganese complex $[Mn_{12}O_{12}(O_2CMe)_{16}(OH_2)_4]$ with an $S_{tot} = 10$ ground state,[3] various derivatives of this so-called Mn_{12} archetype have been investigated,[4] and much effort has been devoted to the synthesis and characterization of new polynuclear clusters that display slow magnetic relaxation below a certain blocking temperature (T_B). There are now many examples of homometal SMMs, mostly containing Mn^{III},[5] but also other metal ions such as V,[6] Fe,[7] Co,[8] or Ni.[9] Still, the Mn_{12} family represented the SMMs with the highest T_B (~3.5 K) and anisotropy barriers U_{eff} (up to 74 K) until 2007, when a Mn_6 complex with enhanced blocking temperature (~4.5 K) and an effective energy barrier to magnetization reversal of 86.4 K was found, the record holder to date.[10,11] Among the essential requirements for SMM behavior are a high-spin ground state S_{tot} and a strong easy axis-type magnetic anisotropy (negative zero-field splitting parameter D_{mol}), which define the energy barrier $U_{eff} \approx |D_{mol}|S_{tot}^2$.[2,12] While impressive progress has been made in terms of increasing S_{tot}, synthetic strategies for manipulating D are a much less developed.[13,14] More recently, it has even been proposed that the anisotropy barrier does not increase with S_{tot} as S_{tot}^2, but the

Received: September 28, 2010
Published: February 18, 2011

dependence is on the order of unity.[15] It has also been questioned whether large magnetic anisotropy and high spin can coexist at all.[16] Given the intrinsic relationship between the S_{tot} and D_{mol} parameters, it was concluded from the latter study that perfect alignment of the Jahn–Teller axes with the largest possible number of paramagnetic centers should be most advantageous for obtaining systems large energy barriers, though this poses a particular challenge for controlling the ferromagnetic exchange. New types of SMMs are thus needed to extend and substantiate the experimental basis in these directions.

Of particular value are families of related complexes with relatively minor, yet controllable perturbations to the structures, since they allow probing the subtle effects of structural or electronic variations on SMM characteristics and, in the end, lead to strategies for the deliberate tuning of SMM properties.[17] Most of the earlier studies had focused on individual high-nuclearity molecules that should, in the ideal case, be well isolated in the crystal lattice for investigating pristine SMM behavior. However, the absence of intermolecular interactions is not a prerequisite for observing a sufficiently large energy barrier to magnetization reversal. In fact, in more recent years various systems that feature intermolecular contacts, either pairwise or in extended arrangements in the crystal lattice, were found to exhibit slow relaxation of the magnetization because of an energy barrier of molecular origin.[18–20] As a new feature it was observed for these systems that the quantum tunnelling of magnetization (QTM) has shifted away from zero field, and hence, they were called "exchange-biased SMMs". Such novel SMMs offer promising prospects for studying the effects of intermolecular interactions on SMM, and it has even been suggested that intermolecular interactions may provide a means of fine-tuning the quantum tunnelling of magnetization in SMMs.[21,22] Modulation of the intermolecular interactions certainly is a challenging task and requires proper adjustment of ligand functionalities in the periphery of the molecular complexes, which emphasizes the particular value of families of robust SMMs with closely related oligometallic core but variable terminal ligand decoration.

The combination of different metal ions in a single cluster for achieving large magnetic anisotropy and high-spin ground states significantly extends the structural landscape for SMMs but has been explored relatively little until now. Mixed 3d/3d transition metal SMMs include $MnCu$,[23] Mn_2Ni_2,[24,25] $Mn_{11}Cr$, Fe_4Ni_4,[26] Mn_6Cr,[27] and Mn_3Ni,[28] some of them showing hysteresis loops with QTM. While targeted synthetic approaches to the construction of SMMs are highly sought after,[27,29] the most common strategy to date for obtaining oligonuclear complexes with SMM behavior is the (more or less serendipity-driven) self-assembly of paramagnetic metal ions and flexible bridging ligands.[30] Diol-type ligands have been particularly successful in this regard,[31] though the variety of ligands in use has remained rather limited. Phenol-pyrazole hybrid ligands have recently emerged as a promising ligand class for high-nuclearity Mn^{III} compounds.[32] On the basis of our experience with pyrazole-derived ligand scaffolds,[33] we have now synthesized a new tridentate diol ligand 2-[3-(2-hydroxyphenyl)-1*H*-pyrazol-1-yl]ethanol (H_2L) with a central pyrazole unit, which gives rise to a new family of heterometal SMMs. These relatively small pentanuclear systems $[Mn_2^{III}Ni_3^{II}L_4(LH)_2X_2(H_2O)_2]$ feature a ferromagnetic $S_{tot} = 7$ ground state, yet sizable anisotropy, and pronounced QTM steps in the hysteresis loops. Here we report and discuss details of the synthesis as well as structural, spectroscopic, and magnetic characterization of two first examples of this new family of SMMs, which are amenable to valuable structural modifications for tuning the SMM behavior.

Scheme 1. Synthesis of H_2L

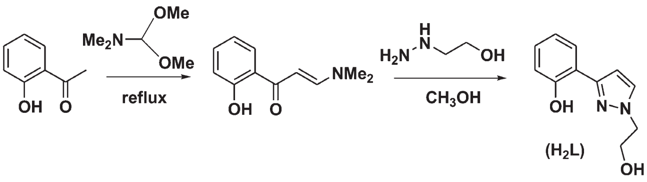

RESULTS AND DISCUSSION

Syntheses and Structural Characterizations. The new ligand 2-{3-(2-hydroxyphenyl)-1*H*-pyrazol-1-yl}ethanol (H_2L) has been synthesized in two steps starting from 2-hydroxyacetophenone (Scheme 1). The intermediate 1-(2-hydroxyphenyl)-3-dimethylaminoprop-2-enone was obtained according to a literature method[34] and was then heated to reflux with excess β-hydroxyethyl hydrazine in methanol solution for 2 h. Extraction of the crude product with light petroleum using a Soxhlet apparatus gave H_2L as needle-shaped white crystals in 40–50% yield. Several design considerations make H_2L an attractive scaffold for assembling oligonuclear complexes: (i) H_2L may act as a tridentate ligand with sufficient flexibility in one arm (the hydroxyethyl subunit); (ii) it provides, after deprotonation, two distinct potential bridging units (phenoxy and alkoxy); and (iii) it is easy to synthesize in reasonable quantities. The molecular structure of H_2L has been determined (see Figure S1 in the Supporting Information). It forms a propeller-like hydrogen-bonded tetramer via the aliphatic OH groups, while the phenolic OH groups are involved in intramolecular hydrogen-bonding to the pyrazole-N.

Reaction of H_2L with $MnX_2 \cdot xH_2O$ (X = Cl, Br) and $NiCl_2 \cdot 6H_2O$ in the presence of NEt_3 in acetonitrile at room temperature gave complexes $[Mn^{III}_2Ni^{II}_3X_2L_4(LH)_2(H_2O)_2]$ (X = Cl: **1**; X = Br: **2**). Both compounds could be crystallized from dichloromethane solutions as **1**$\cdot 8CH_2Cl_2$ or **2**$\cdot 8CH_2Cl_2$, respectively. In both cases the complexes crystallize in the triclinic space group $P\bar{1}$ as quasi-linear centrosymmetric Mn–Ni–Ni–Ni–Mn molecules, with the central nickel atom situated on a center of inversion. Overall molecular topologies determined by X-ray crystallography are very similar, and complex **2** is shown as a representative example in Figure 1 (the molecular structure of **1** is shown in Figure S2). Relevant atom distances and bond angles are collected in Table 1.

Both complexes contain a $[Mn_2Ni_3(\mu\text{-}O)_8]$ core where the coordination number of all metal atoms is six and the coordination environment is more or less distorted octahedral. Complexes **1** and **2** differ only by the terminal ligands bound to Mn, which are either Cl in **1** or Br in **2**. Oxidation states of the metal ions, Mn^{III} and Ni^{II}, are confirmed by bond valence sum calculations[35] and by the relatively short bonds for the Mn^{III} ions (see Table 1). The string of metal ions can be best visualized as five edge-sharing octahedra (Figure 2, bottom). The three Ni^{II} ions are doubly bridged by phenoxy-O atoms, while both peripheral Mn^{III} ions are linked to the Ni^{II}_3 core via double alkoxy-O bridging. Mn^{III} ions are found in $\{NO_4X\}$ environment with equatorial position occupied by the {ONO} donor site of a tridentate ligand $[L]^{2-}$ and an alkoxo-O of another ligand, and with the terminal halide (Cl or Br) and a water molecule in the axial positions. As expected, the Mn^{III} ions exhibit a strong Jahn–Teller elongation along the Cl/Br–Mn–OH_2 axis (Figure 2, top) with Mn–O/Cl distances of 2.34/2.61 Å in **1**$\cdot 8CH_2Cl_2$ and

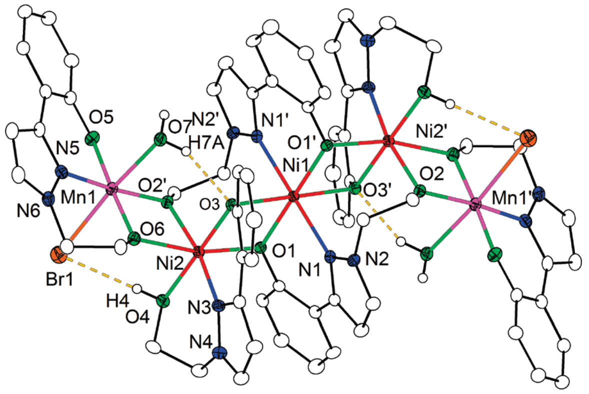

Figure 1. Molecular structure of complex **2** in **2**·8CH$_2$Cl$_2$ (thermal ellipsoids drawn at the 30% probability level). Most hydrogen atoms and solvent molecules are omitted for clarity. Symmetry transformation used to generate equivalent atoms: (′) 1−*x*, 1−*y*, 1−*z*.

Table 1. Selected Distances [Å] and Angles [deg] for 1·8CH$_2$Cl$_2$ and 2·8CH$_2$Cl$_2$.[a,b]

	1·8CH$_2$Cl$_2$	**2**·8CH$_2$Cl$_2$
Ni1−N1	2.173(7)	2.186(4)
Ni1−O1	2.030(6)	2.026(3)
Ni1−O3	2.120(6)	2.116(3)
Ni2−N3	2.022(7)	2.030(4)
Ni2−O1	2.014(6)	2.012(3)
Ni2−O2′	2.062(6)	2.065(3)
Ni2−O3	2.061(6)	2.056(3)
Ni2−O4	2.121(6)	2.127(3)
Ni2−O6	2.043(6)	2.047(3)
Mn1−N5	1.977(7)	1.994(4)
Mn1−O2′	1.889(6)	1.891(3)
Mn1−O5	1.872(6)	1.866(4)
Mn1−O6	1.888(6)	1.886(3)
Mn1−O7	2.344(6)	2.337(4)
Mn1−X1	2.609(3)	2.7775(9)
Ni1···Ni2	3.1089(11)	3.1106(6)
Ni2···Mn1	3.0447(17)	3.0457(10)
O4···X1	3.17(1)	3.238(4)
O7···O3	2.77(1)	2.757(5)
N1−Ni1−N1′	180	180
O1−Ni1−O1′	180	180
O3−Ni1−O3′	180	180
N3−Ni2−O2′	171.7(3)	170.5(1)
O1−Ni2−O6	164.7(2)	165.0(1)
O3−Ni2−O4	177.9(2)	178.9(1)
N5−Mn1−O2′	167.2(3)	169.4(2)
O5−Mn1−O6	175.9(3)	177.6(2)
O7−Mn1−X1	175.4(2)	174.5(1)
O4−H4···X1	−	175(5)
O7−H7A···O3	−	154(7)

[a] Symmetry transformation used to generate equivalent atoms: (′) 1−*x*, 1−*y*, 1−*z*. [b] X = Cl: **1**; X = Br: **2**

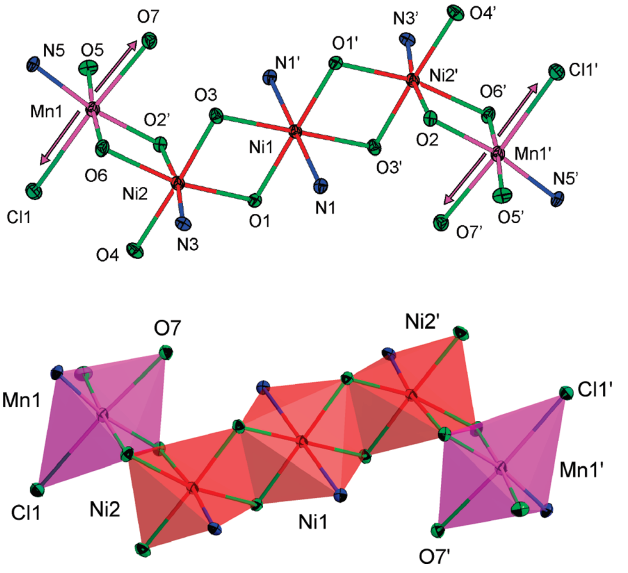

Figure 2. (Top) Coordination environment of the metal atoms in **1**. The arrows emphasize the Jahn−Teller axes. Symmetry transformation used to generate equivalent atoms: (′) 1−*x*, 1−*y*, 1−*z*. (Bottom) Emphasis of the five edge-sharing octahedral of the Mn^{III}−Ni^{II}−Ni^{II}−Ni^{II}−Mn^{III} core.

Mn−O/Br distances of 2.34/2.78 Å in **2**·8CH$_2$Cl$_2$. In case of nickel the octahedral environment is more regular with the central Ni^{II} featuring a $\{N_2O_4\}$ and the other two Ni^{II} ions a $\{NO_5\}$ coordination sphere. Interestingly, two of the six pyrazole-based ligands in **1** and **2** are only deprotonated once. The remaining neutral alcohol function of these partially deprotonated [HL]$^-$ serves as a terminal ligand to the Ni$^{II}_3$ core and exhibits a strong intramolecular H-bond to the neighboring Mn-bound halide ion [d(O4···Cl1) = 3.17(1) Å in **1**·8CH$_2$Cl$_2$; d(O4···Br1) = 3.238(4) Å in **2**·8CH$_2$Cl$_2$];[36] the Ni−O4 bond is elongated compared to all other Ni2−O and Ni2−N bonds (2.10−2.13 Å versus 2.01−2.07 Å). Another important intramolecular H-bond involves the Mn^{III}-bound water and the proximate phenolato-O3 atom [d(O7···O3) ≈ 2.76 Å]. These two H-bonding interactions displayed by the axial ligands at Mn fix the Cl/Br−Mn−OH$_2$ axis relative to the O3−Ni2−O4 axis; i.e., the Mn1 and Ni2 coordination octahedra have their elongated axes aligned parallel. With respect to the magnetic properties it is also important to note that the Jahn−Teller axes of the Mn^{III} ions at both ends of the Mn^{III}−Ni^{II}−Ni^{II}−Ni^{II}−Mn^{III} core are roughly parallel to each other.

Magnetic and EPR Properties. Magnetic properties of **1** and **2** were investigated using a commercial SQUID MPMS system as well as a homemade micro-Hall-bar magnetometer.[37] The result of SQUID susceptibility measurements of a powder sample of **1** at magnetic field values of 0.5, 1, and 5 T in a temperature range between 2 and 300 K are shown in Figure 3.

Above 250 K, the χT value is about 11.5 K cm^3 mol^{-1} and is nearly temperature independent, in accordance with the presence of two high-spin Mn^{III} ($S = 2$) and three Ni^{II} ($S = 1$). At low temperatures, the sharp increase of the susceptibility to around 25 K cm^3 mol^{-1} is an indication for ferromagnetic intramolecular coupling. An effective Heisenberg Hamiltonian of the form

$$H = -J_1(S_{Mn1}S_{Ni1} + S_{Mn2}S_{Ni3}) - J_2(S_{Ni1}S_{Ni2} + S_{Ni2}S_{Ni3}) \qquad (1)$$

was used to fit the data. From the numerically calculated best fit, shown as red lines in Figure 3, $J_1 \approx 46$ K for the Mn−Ni coupling

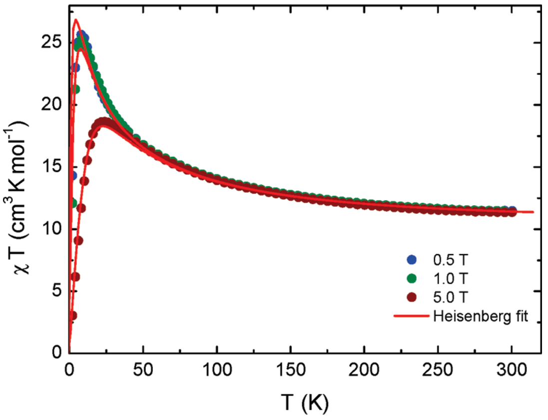

Figure 3. Temperature dependence of χT for a microcrystalline sample of **1**. The various fields are indicated in the inset. The red line is a Heisenberg fit to the data (see text).

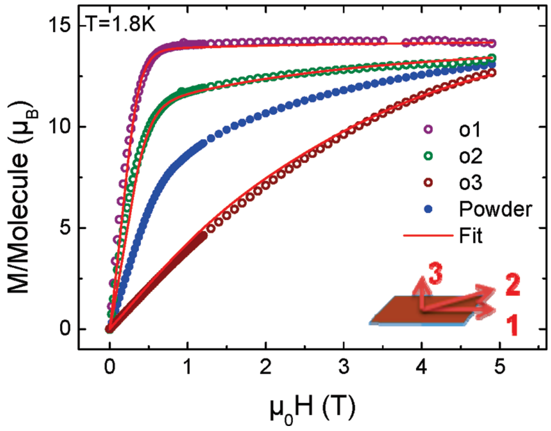

Figure 4. Magnetization versus field data for different orientations of a single crystal of $\mathbf{1}\cdot 8CH_2Cl_2$ at 1.8 K and the corresponding powder data. The red lines represent best fits. The inset shows a top view of a typical crystal. o1, o2, o3 are the three different orientations indicated by the sketch in the inset.

and $J_2 \approx 22$ K for the Ni−Ni coupling were obtained with an average g factor $g_{av} = 2.06$; the latter value is in a good agreement with the value directly measured by ESR, $g_{av}(ESR) = 2.08$ (see below). Obviously the quasi-linear $[Mn^{III}Ni^{II}Ni^{II}Ni^{II}Mn^{III}]$ is a purely ferromagnetically coupled system with a ground-state spin of $S_{tot} = 7$.

The results of variable field magnetization measurements for a polycrystalline sample and for a single crystal of $\mathbf{1}\cdot 8CH_2Cl_2$ with different field orientations are shown in Figure 4. While the magnetization of the powder sample and of the single-crystal sample at orientations o2 and o3 is not saturated at a field of 5 T, the crystal oriented along o1 saturates already at about 0.6 T. From the saturation value $M_S \approx 14.2\ \mu_B$ one can again derive a spin ground state of $S_{tot} = 7$, assuming $g_{av} = 2.03$. This g_{av} value, though slightly smaller, is reasonably consistent with the values obtained from the powder susceptibility and ESR data. The total g_{av} factor deviates from the value of 2.0 that is characteristic for Mn^{III} because of the contribution from Ni^{II}, which usually has g values in the range 2.2−2.3.[38]

Since the magnetization measurements, presented in Figure 4, have been performed at a temperature much lower than the estimated strength of intramolecular couplings J_1 and J_2 (see eq 1), one can assume that only the ground-state multiplet $S_{tot} = 7$ is populated. The first exited multiplet which is sufficiently well separated from the ground state due to large values of J_1 and J_2 does not contribute to the magnetization in this case. Therefore, for the analysis of these data an effective spin Hamiltonian for the total ground state spin $S_{tot} = 7$ in the form

$$H = D\left(S_z^2 - \frac{1}{3}\, S(S+1)\right) + E(S_x^2 - S_y^2) + g\mu_B\, \vec{H}\cdot \vec{S} \qquad (2)$$

can be applied. From a numerical fit of this equation to the data, we were able to obtain a rough value for the uniaxial anisotropy parameter $D_{mol} \approx -0.5$ K. Within this framework, one can get an estimation for the effective energy barrier for spin reversal of $U_{eff} = |D_{mol}|S_{tot}^2 \approx 25$ K. Unfortunately, it was not possible to determine a reliable value of the E parameter with this method, as the sample crystals were rather small (~20 μg) and very thin. Furthermore, the softness of the crystal made it almost impossible to align them with the necessary angular precision. However, from the measurements it can be estimated $10\cdot|E| \leq |D|$, which gives an upper limit for $|E|$ of 45 mK.

Figure 5 shows an ac susceptibility measurement of a polycrystalline sample of $\mathbf{1}\cdot 8CH_2Cl_2$ with a so-called Cole−Cole (Argand) plot in the inset. The dispersion data presented in this way reveal an almost perfect semicircle. This is clear evidence of a relaxation process with a single relaxation time τ_0[39] and suggests SMM behavior of $\mathbf{1}\cdot 8CH_2Cl_2$.

Similar measurements were also performed for $\mathbf{2}\cdot 8CH_2Cl_2$ (see Figures S4−S6 for variable-temperature and variable-field SQUID data as well as ac susceptibility for a polycrystalline sample). For $\mathbf{2}\cdot 8CH_2Cl_2$ coupling constants $J_1 \approx 42$ K (for Mn−Ni) and $J_2 \approx 18$ K (for Ni−Ni) were found, again with a spin ground state of $S_{tot} = 7$. From the single-crystal measurements it was possible to estimate a uniaxial anisotropy parameter $D_{mol} \approx -0.4(5)$ K, which is well comparable with the result for complex **1**.

High-field electron spin resonance (HF-ESR) measurements in magnetic fields up to 15 T were performed on an oriented powder sample of $\mathbf{1}\cdot 8CH_2Cl_2$. Owing to a strong magnetic anisotropy (see below) the single-crystalline powder particles in the sample were aligned in the magnetic field along their crystalline magnetic anisotropy axis. A typical ESR spectrum at a frequency ν of 332 GHz and $T = 20$ K is shown in Figure 6. The spectrum features a relatively simple structure consisting of seven well-defined and almost equally spaced absorption lines with a separation of the resonance fields B_{res} by ~1 T. The intensity of the lines continuously decreases with increasing the magnetic field strength. Measurements at different excitation frequencies reveal a linear relationship between ν and B_{res} for each absorption line. The respective ν vs B_{res} dependencies (resonance branches) are plotted together in Figure 6. The slope $d\nu/dB$ of all resonance branches is almost identical. This enables a straightforward determination of $g = (h/\mu_B)d\nu/dB = 2.08$, which is in very good accordance with the values for $\mathbf{1}\cdot 8CH_2Cl_2$ derived from the SQUID measurements. As shown in Figure 6 the extrapolation of the $\nu(B_{res})$ dependence of the leftmost line in the ESR spectrum (line 1) to zero magnetic field yields the magnitude of the magnetic anisotropy gap Δ, which is 150 GHz (7.2 K). Since Δ is related to the anisotropy parameter D_{mol} of the molecular complex as $|D_{mol}| = \Delta/[S_{tot}^2 - (S_{tot} - 1)^2]$, with $S_{tot} = 7$ one obtains the absolute value $|D_{mol}| = 11$ GHz (0.55 K) for $\mathbf{1}\cdot 8CH_2Cl_2$.[40,33b] This value again is in good agreement with the value derived from magnetization data.

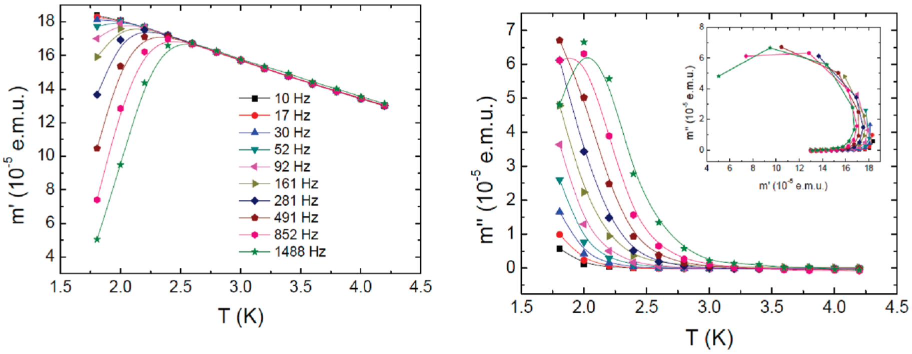

Figure 5. Plots of in-phase (m′, left) and out-of-phase (m″, right) ac susceptibility versus temperature for a microcrystalline sample of $\mathbf{1}\cdot 8CH_2Cl_2$. The data were collected in an ac field of 2.56 Oe oscillating at the indicated frequencies. The inset in the right graph shows a Cole−Cole plot (m″ versus m′).

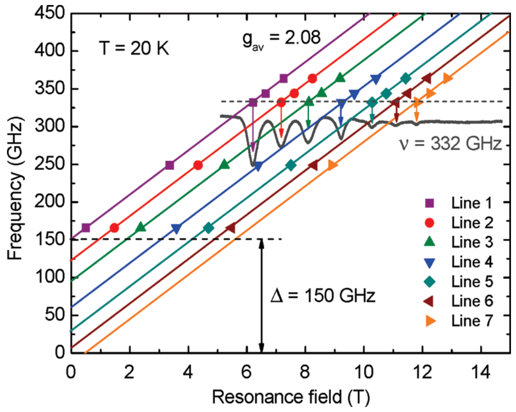

Figure 6. Frequency ν versus resonance magnetic field B_{res} dependence of the ESR lines (symbols) and a representative ESR spectrum of $\mathbf{1}\cdot 8CH_2Cl_2$ at T = 20 K. Solid lines are linear fits to the experimental data points. Inset: Comparison of the experimental and modeled ESR spectra (see text).

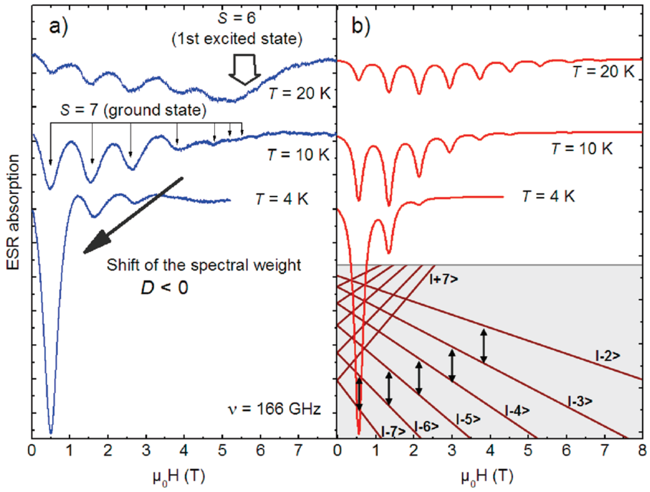

Figure 7. Temperature dependence of the ESR spectra of $\mathbf{1}\cdot 8CH_2Cl_2$ at ν = 166 GHz. (a) Experimentally obtained ESR spectra; (b) calculated ESR spectra and energy levels (see text).

The sign of D_{mol} can be unambiguously determined from the temperature dependence of the ESR spectrum which is presented in Figure 7a. Here, one observes a clear shift of the spectral weight to lower magnetic fields at low temperatures, whereas the positions of the absorptions do not change. Such redistribution of the ESR spectral weight occurs in the case of a spin doublet ground state $|\pm S_{tot}^{Z}\rangle$ corresponding to the *negative* sign of D_{mol}, whereas for the case of a singlet state $|0\rangle$, i.e. for a positive sign of D_{mol}, the spectral weight should shift to higher fields.[33b] This is illustrated by the energy level diagram in Figure 7b where, for $D_{mol} < 0$ at low temperatures, only the lowest state $|-7\rangle$ is sufficiently populated, yielding the strongest intensity for the leftmost line in the ESR spectrum. Thus, the HF-ESR results give clear evidence for a bi-stable ‘easy axis’ ground state of $\mathbf{1}\cdot 8CH_2Cl_2$ with a substantial anisotropy barrier $U = S_{tot}^{2}|D_{mol}|$ = 27 K between two degenerate ground states $S_{tot}^{Z} = +7$ and $S_{tot}^{Z} = -7$.

With the parameters obtained from the above analysis the ESR spectrum of $\mathbf{1}\cdot 8CH_2Cl_2$ was modeled using the EasySpin toolbox for Matlab[41] for the case of the parallel orientation of the ‘easy axis’ of the complex to the direction of the magnetic field, i.e. the situation that is expected for the oriented powder sample. This model, according to eq 2, describes only the ground state of the molecule while neglecting the excited higher-energy spin states. As can be seen in Figure 7 the simulation captures well the main features of the experimentally observed ESR spectrum: the extent of the fine structure of the spectrum, the number of lines, and their relative intensities. Discrepancies between the model and the experiment could be due to a nonperfect alignment of the powder particles as well as to the simplifications of the model that neglects intermolecular interaction. Beyond this model description in the experimental ESR spectrum at T = 20 K an additional wide absorption line emerges at around 5.5 T (see Figure 7a), which can most probably be attributed to transitions inside the higher-energy spin multiplets.

To confirm further the SMM properties of **1** and **2** a micro-Hall-bar magnetometer was used for low-temperature single-crystal magnetization measurements. The crystals were oriented with the easy axis approximately parallel to the applied magnetic field. Measurements were performed at several temperatures in the range of 0.3−2.0 K, and sweep rates in the range of 12−200 mT s^{-1}. The left parts of Figures 8 and 9 show hysteresis loops of $\mathbf{1}\cdot 8CH_2Cl_2$ and $\mathbf{2}\cdot 8CH_2Cl_2$ with a constant field sweep rate at different temperatures. For both complexes, hysteretic behavior was observed below a temperature T_B of approximately 1.5 K. The sweep rate dependence is depicted in the right parts of Figures 8 and 9. Both compounds show sharp QTM steps, which are particularly pronounced for $\mathbf{1}\cdot 8CH_2Cl_2$. An exemplary low-temperature hysteresis loop of $\mathbf{1}\cdot 8CH_2Cl_2$ measured at 300 mK

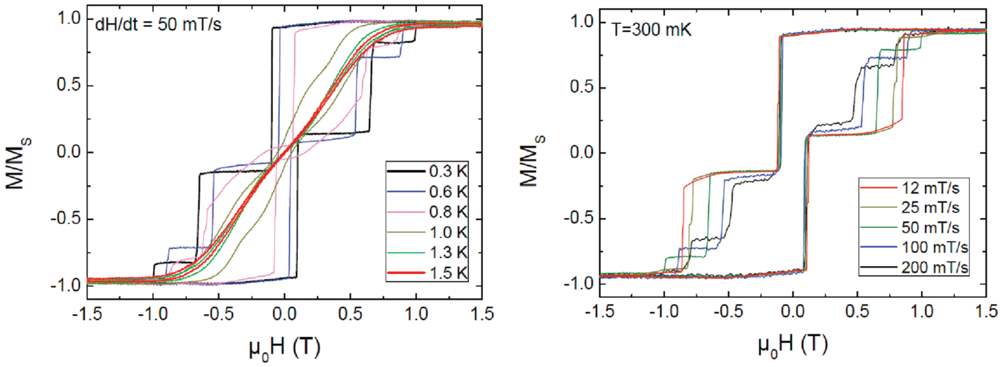

Figure 8. Magnetization (M) versus dc field hysteresis loops for a single crystal of **1**·8CH$_2$Cl$_2$ at constant sweep rate and variable temperature (left) and constant temperature and variable sweep rate (right).

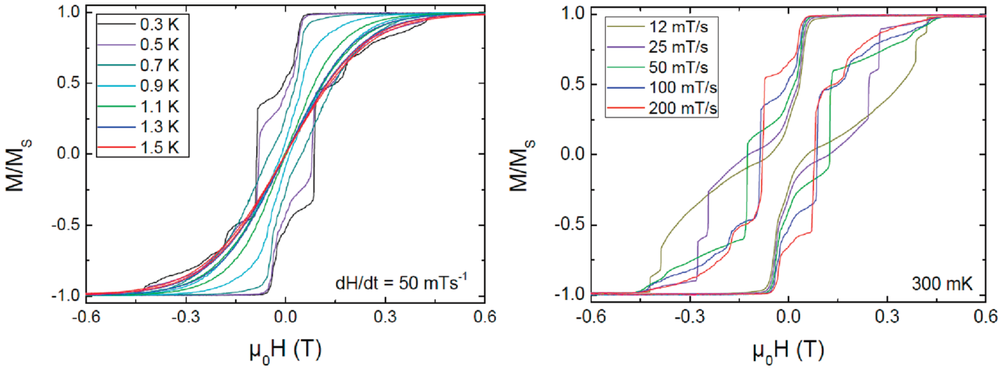

Figure 9. Magnetization (M) versus dc field hysteresis loops for a single crystal of **2**·8CH$_2$Cl$_2$ at constant sweep rate (left) and at a constant temperature of 300 mK and different field scan rates (right).

with the field sweep rate of 200 mT/s is compared in Figure 10 with the energy scheme of the spin levels of the ground state multiplet. The scheme was calculated using the simplest model (eq 2), with the parameters taken from the SQUID and ESR measurements ($S_{\text{tot}} = 7$; $D_{\text{mol}} = -0.55$ K; $g_{\text{av}} = 2.08$). The model qualitatively describes the main features of the magnetization behavior such as the number and approximate positions of the relaxation steps which correspond to the level crossing points in the diagram. The correspondence between the crossing points and the positions of the steps that indicate the flip of the magnetization vector due to the quantum tunneling is closest for the highest sweep rate of the magnetization measurement and gets worse for smaller sweep rates. Indeed, the rate of the spin flips in the ESR experiment determined by the excitation frequency is by orders of magnitude higher. Thus, the level diagram derived from the ESR data should correspond to a magnetization measurement performed at a virtually infinite sweep rate.

However, despite similar model parameters the overall shape of the hysteresis loops look quite different for **1**·8CH$_2$Cl$_2$ and **2**·8CH$_2$Cl$_2$. In particular, in the case of **1**·8CH$_2$Cl$_2$ the first relaxation step in the hysteresis loop is above the zero crossing of the magnetic field, while in the case of **2**·8CH$_2$Cl$_2$ it is below the zero crossing. It is reasonable to assume that these features are mainly determined by relaxation paths caused by intermolecular interactions, with ferromagnetic intermolecular interactions in the case of **1**·8CH$_2$Cl$_2$ and predominantly antiferromagnetic interactions in the case of **2**·8CH$_2$Cl$_2$.[19] The interaction

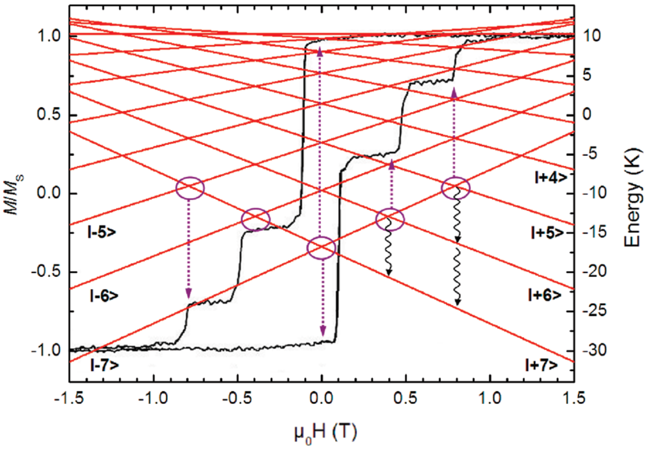

Figure 10. Magnetization vs dc field hysteresis loops for a single crystal of **1**·8CH$_2$Cl$_2$ at a temperature of 300 mK and the field sweep rate of 200 mT/s (black line) and the calculated energy level scheme.

between two neighboring molecules can be described by a simple effective interaction Hamiltonian

$$H_{\text{D}} = \sum_{i=1,2} (DS_{iz}{}^2 + g\mu_{\text{b}}\mu_0 S_{iz}H_z) - J_{12}S_1S_2$$

Within this framework, one can estimate the intermolecular coupling interactions for both systems by the following equation:[18]

$$J \approx -\frac{g\mu_b\mu_0 HS}{S^2}$$

This leads to a value for J of around 25 mK (ferromagnetic) for **1** and −35 mK (anitferromagnetic) for **2**. Within this simplified dimer model the zero field step and some further steps of the hysteresis loops at higher field can be described, but not all of them. To fully describe the hysteresis features one would need to extend this model to a chain of more than two molecules interacting with each other. At the moment, however, it is not possible to accurately simulate this extended intermolecular coupling scheme because the dimension of the resulting Hamiltonian exceeds the memory capacity of currently available computers. It is possibly owing to the relative smallness of the intermolecular interactions and broadness of the absorption lines that the ESR spectra do not exhibit any characteristic splitting of the resonance lines due to the exchange bias.[19]

Table 2. Selected Intermolecular Distances [Å] for $\mathbf{1\cdot 8CH_2Cl_2}$ and $\mathbf{2\cdot 8CH_2Cl_2}$

atom1	atom2	symm. op. 1	symm. op. 2	distance	length−vdW
$1\cdot 8CH_2Cl_2$:					
Cl1	H61A	x, y, z	$1-x, 1-y, 2-z$	2.664	−0.286
O5	H62A	x, y, z	$1-x, 1-y, 2-z$	2.401	−0.319
O7	H64B	x, y, z	$x, 1+y, z$	2.385	−0.335
Cl4	H46	x, y, z	$1-x, 2-y, 2-z$	2.935	−0.015
Cl2	H61B	x, y, z	x, y, z	2.894	−0.056
Cl3	H43	x, y, z	$-1+x, -1+y, z$	2.737	−0.213
Cl2	H61B	x, y, z	$1-x, 1-y, 2-z$	2.872	−0.078
Cl7	H51B	x, y, z	$-1+x, y, z$	2.926	−0.024
$2\cdot 8CH_2Cl_2$:					
Br1	H31A	x, y, z	$2-x, 1-y, 2-z$	3.035	−0.015
Br1	H41	x, y, z	$2-x, 2-y, 2-z$	2.998	−0.052
Br1	H61B	x, y, z	$1-x, 1-y, 2-z$	2.992	−0.058
Br1	H62B	x, y, z	$1-x, 1-y, 2-z$	3.022	−0.028
O5	H62B	x, y, z	$1-x, 1-y, 2-z$	2.456	−0.264
O7	H64A	x, y, z	$x, 1+y, z$	2.579	−0.141
Cl2	H61B	x, y, z	x, y, z	2.947	−0.003
Cl3	H43	x, y, z	$-1+x, -1+y, z$	2.849	−0.101

Intermolecular Interactions. In view of the importance of weak intermolecular interactions for the QTM properties of SMMs and the differing characteristics of **1** and **2**, we have taken a closer look at the crystal packing and intermolecular contacts of the new $\{Mn_2Ni_3\}$ compounds. One should note that $\mathbf{1}\cdot 8CH_2Cl_2$ and $\mathbf{2}\cdot 8CH_2Cl_2$ are isostructural, and hence there are only minor differences. Classic hydrogen bonds in $\mathbf{1}\cdot 8CH_2Cl_2$ and $\mathbf{2}\cdot 8CH_2Cl_2$ are all intramolecular (as described above), but additional intermolecular interaction might occur via short C−H···X (X = Cl, Br, O) contacts, of which several are observed in the crystal structures. In this context short contacts are defined as a distance shorter than the sum of the van der Waals radii of the respective atoms with a C−H···X angle greater than 90°. Such distances were determined using the program Mercury[42] and are listed in Table 2.

Interestingly, within the given range no direct molecular contacts of two or more $[Mn^{III}{}_2Ni^{II}{}_3Cl_2L_4(LH)_2(H_2O)_2]$ units are observed for $\mathbf{1}\cdot 8CH_2Cl_2$. Instead the CH_2Cl_2 solvent molecules containing the atoms Cl2/3 and Cl4/5 provide interactions to neighboring molecules **1** via a network of C−H···X (X = Cl, O) contacts (Figure 11). However, H-atoms from neighboring $[Mn^{III}{}_2Ni^{II}{}_3Cl_2L_4(LH)_2(H_2O)_2]$ molecules are not too far away. The closest contact between the manganese-bound chlorine atom and the next H-atom of a surrounding $[Mn^{III}{}_2Ni^{II}{}_3Cl_2L_4(LH)_2(H_2O)_2]$ moiety is 3.013 Å (Cl1···H41−C41[$2-x$,$2-y$,$2-z$]); the latter belongs to a pyrazole group. In case of $\mathbf{2}\cdot 8CH_2Cl_2$ two short contacts of the bromine atom of one $[Mn^{III}{}_2Ni^{II}{}_3Br_2L_4(LH)_2(H_2O)_2]$ to close-by hydrogen atoms H−C (H31A and H41) result in direct contacts to the neighboring $[Mn^{III}{}_2Ni^{II}{}_3Br_2L_4(LH)_2(H_2O)_2]$ molecules. Additional intermolecular contacts via solvent molecules containing Cl2/Cl3 are present as well (Figure 12).

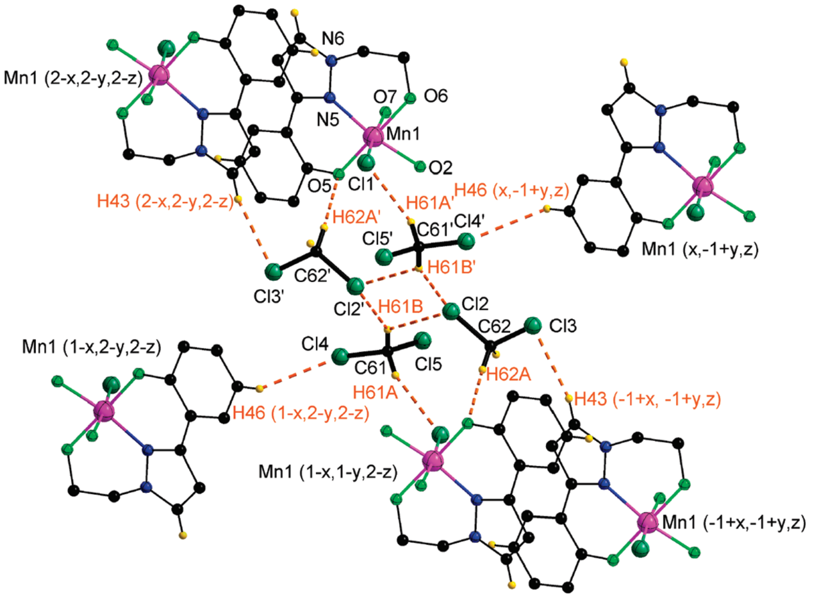

Figure 11. Emphasis of some intermolecular C−H···X contacts in $\mathbf{1}\cdot 8CH_2Cl_2$. Symmetry transformation used to generate equivalent atoms: (′) $1-x$, $1-y$, $2-z$. Other symmetry transformations are given in the figure.

It seems that in both compounds at least one close intermolecular contact between individual $[Mn^{III}_2Ni^{II}_3X_2L_4(LH)_2(H_2O)_2]$ molecules is present that involves the manganese-bound halide atom and the hydrogen atom of a neighboring pyrazole group, namely H41. Since a center of inversion is present within each molecule a one-dimensional (1D) chainlike arrangement is formed within the crystal (Figure 13). However, this contact is shorter than the sum of the van der Waals radii only in the case of **2**·8CH$_2$Cl$_2$. One might thus speculate that this contact, because of the larger bromine atom, serves as the dominant exchange pathway in **2**·8CH$_2$Cl$_2$, mediating an antiferromagnetic interaction, whereas it is negligible in **1**·8CH$_2$Cl$_2$. In the latter case exchange interactions are thus weaker (see the lower absolute value: +25 mK for **1** and −35 mK for **2**) and are mainly mediated indirectly via CH$_2$Cl$_2$ solvent molecules in the crystal lattice, or dipolar interactions through space, resulting in a ferromagnetic situation. It should be kept in mind though that this is a rather reductionistic treatment that should be considered with care, since the intermolecular C−H···X contact involving H41 is only one (albeit the most obvious) of several intermolecular interactions which, as a whole, build up the 3D crystal structure.

The H-bonding contacts in **1**·8CH$_2$Cl$_2$ and in **2**·8CH$_2$Cl$_2$ seem to be further supported by $\pi-\pi$ ring interactions. Close inspection of the rings containing the atoms N5, N6, C41−C43 (pyrazole part of the ligand), and C44−C49 (phenol part of the ligand, excluding O) reveals the possibility for such intermolecular interactions. Relevant parameters were calculated with the program PLATON[43] and are listed in Table 3. Values are rather similar and show an almost parallel alignment of both rings (∠P1−P2 in Table 3). The distance of both ring-centroids is approximately 3.8 Å, but they are displaced relative to each other, which is reflected by the angle between the Cg(1)−Cg(2) vector and the normal to one of the planes formed by the ring atoms (∠CgCg−P in Table 3). Hence, the rings are offset in such a way that a ring atom almost lies over the center of the other ring. This is a rather common situation in complexes with aromatic nitrogen heterocycles and reveals that such an arrangement also has a contribution from $\pi-\sigma$ attraction.[44] It is important for the present discussion, however, that metric parameters collected in Table 3 are rather similar for **1**·8CH$_2$Cl$_2$ and in **2**·8CH$_2$Cl$_2$ and, at the present stage of knowledge, cannot rationalize the different magnetic properties of the two compounds.

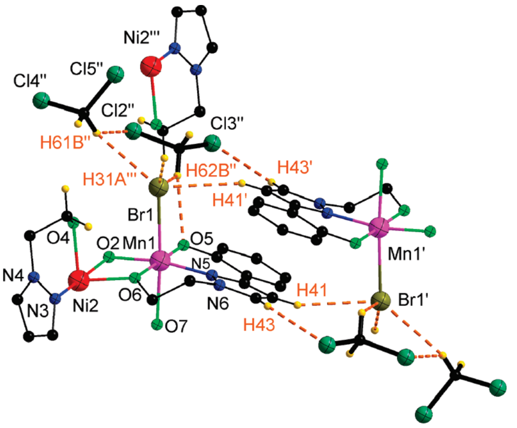

Figure 12. Emphasis of some intermolecular C−H···X contacts in **2**·8CH$_2$Cl$_2$. Symmetry transformations used to generate equivalent atoms: (′) 2−*x*, 2−*y*, 2−*z*, (″) 1−*x*, 1−*y*, 2−*z*, (‴) 2−*x*, 1−*y*, 2−*z*.

CONCLUSIONS

The new diprotic and potentially tridentate ligand H$_2$L allowed to synthesize and characterize first members of a new family of heterometallic $Mn^{III}_2Ni^{II}_3$ complexes that exhibit a robust quasi-linear structure supported by various intramolecular hydrogen bonds, with variable terminal ligands X (Cl and Br in the case of **1** and **2**). These complexes exhibit relatively strong intramolecular ferromagnetic coupling via the alkoxo and phenoxo O atoms, giving an $S_{tot} = 7$ ground state, and sizable uniaxial anisotropy that is reinforced structurally by the intramolecular hydrogen bonds fixing the elongated Jahn−Teller axes of the individual coordination polyhedra roughly parallel. Hence these new complexes show properties typical for SMM behavior, with an energy barrier to thermal relaxation of the magnetization of 27 K (**1**) or 22 K (**2**). Noteworthy are the pronounced QTM steps in the hysteresis curve of the magnetization, which are, however, distinctly different for **1** and **2** since QTM between the ground states does not occur at static zero field but is shifted to positive (**1**) or negative (**2**) fields. This is likely due to intermolecular contacts between the individual SMM units, causing the quantized energy sublevels of the molecules to interact coherently and produce superposition states.[17,18,22] Such opposed exchange bias for the two complexes, viz. ferromagnetic for **1**·8CH$_2$Cl$_2$ but antiferromagnetic for **2**·8CH$_2$Cl$_2$, is surprising, given that **1**·8CH$_2$Cl$_2$ and **2**·8CH$_2$Cl$_2$ are isostructural. Close inspection of the crystal packing reveals only subtle differences, which are mainly due to the different size of the peripheral Cl versus Br ligands at Mn^{III} and the resulting extent of C−H···X (X = Cl, Br) contacts with neighboring molecules. These interactions through C−H···X hydrogen bonds, albeit very weak, might possibly be responsible for the significant effect on the quantum properties of these SMMs, which shows that at the present stage of knowledge and the inherent difficulties associated with crystal

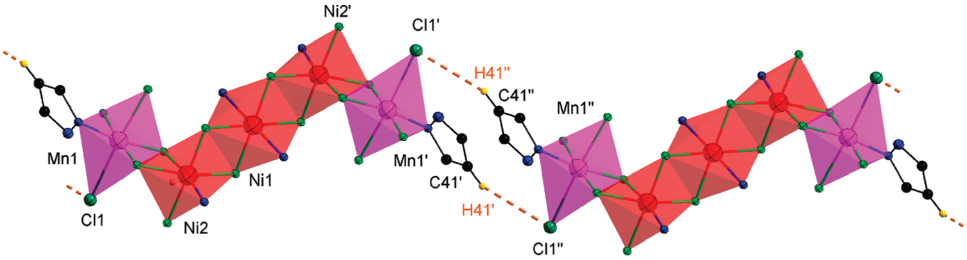

Figure 13. Emphasis of intermolecular C−H···Cl contacts in **1**·8CH$_2$Cl$_2$. Symmetry transformations used to generate equivalent atoms: (′) 1−*x*, 1−*y*, 1−*z*, (″) −1+*x*, −1+*y*, −1+*z*.

Table 3. Parameters for Selected Short Ring Interactions for $1\cdot 8CH_2Cl_2$ and $2\cdot 8CH_2Cl_2$.[a]

	d(Cg1−Cg2) [Å][b]	∠P1−P2 [deg][c]	d(Cg1−P2) [Å]/d(Cg2−P1) [Å][d]	∠CgCg−P2 [deg]/∠CgCg−P1 [deg][e]
$1\cdot 8CH_2Cl_2$:	3.860	4.4	3.311/3.197	34.1/30.9
$2\cdot 8CH_2Cl_2$:	3.818	6.8	3.336/3.130	34.9/29.1

[a] 1 = N5, N6, C41−C43 [*x*, *y*, *z*], 2 = C44−C49 [2−*x*, 2−*y*, 2−*z*], Cg = ring-centroid, P = plane. [b] Distance between Cg. [c] Angle between P. [d] Perpendicular distance of Cg(*x*) on ring (*y*). [e] Angle Cg(1)−Cg(2) vector and normal to P.

engineering any full control of inter-SMM interactions is still far beyond the means of the chemist.

Attractive features of this family of SMMs, which are relevant to further investigations toward the targeted modulation of SMM properties, are (i) the robustness of the Mn_2Ni_3 core that is reinforced by the intramolecular hydrogen bonds, minimizing structural distortions of the $Mn^{III}{}_2Ni^{II}{}_3$ SMM building blocks; (ii) the relatively strong intramolecular ferromagnetic coupling that separates excites states from the $S_{tot} = 7$ ground state; (iii) the pronounced QTM steps in the hysteresis curves, and (iv) the possibility of exchanging the terminal ligands X at the outer Mn^{III} ions. In fact, variation of the peripheral ligands X, including bridging ligands that establish direct linkages between the individual complex units, should allow the rational assembly of 1D chains of heterometallic SMMs[45] and a more detailed study of the effect of intermolecular interactions (and hence the exchange bias) in such correlated systems. Studies in this direction are ongoing in our laboratories.

EXPERIMENTAL SECTION

General Procedures and Materials. All manipulations were performed under aerobic conditions using chemicals and solvents as received unless otherwise stated. 1-(2-Hydroxyphenyl)-3-dimethylaminoprop-2-enone as a precursor of the ligand H_2L was synthesized as described elsewhere.[34]

Synthesis of 2-[3-(2-Hydroxyphenyl)-1H-pyrazol-1-yl]ethanol (H_2L). A mixture of 1-(2-hydroxyphenyl)-3-dimethylaminoprop-2-enone (20 g, 0.104 mol) and 2-hydroxyethyl hydrazine (29.3 g, 0.384 mol) in methanol (100 mL) was heated to reflux with stirring for 3 h. Then the methanolic solution was poured on ice, and the resulting brown precipitate was isolated by filtration and dried in air. The crude product was purified by Soxhlet extraction with light petroleum over several days to give H_2L as needle-shaped white crystals. Yield: 9.3 g (0.045 mol, 44%). Mp 91 °C. ^1H NMR (500 MHz, DMSO-d_6): δ 10.68 (s, Ar−OH), 7.84 (d, 1H, *J* = 2.5 Hz), 7.70 (dd, 1H, *J* = 7.5, 1.5 Hz), 7.15 (ddd, 1H, *J* = 1.5, 6.75, and 8.5 Hz), 6.89 (dd, 1H, *J* = 1 Hz, 8 Hz), 6.87 (dd, 1H, *J* = 1 Hz, 7.5 Hz), 6.85 (d, 1H, *J* = 1 Hz), 4.93 (t, 1H, *J* = 5 Hz), 4.22 (t, 2H, *J* = 5.5 Hz), 3.77 (q, 2H, *J* = 5.5 Hz) ppm. $^{13}C\{^1H\}$ NMR (125.75 MHz, DMSO-d_6): δ 154.9, 149.7, 132.1, 128.6, 126.6, 119.2, 117.2, 116.4, 102.5, 59.8, 54.1 ppm. MS (EI): *m*/*z* (%) = 205 (20), $[M + H]^+$, 204 (100), $[M]^+$, 173 (80), $[M - CH_2OH]$, 160 (40), $[M - CH_2CH_2O]$. IR (KBr): $\tilde{\nu}$ 33478 (w), 3325 (br), 3015 (w), 2958 (w), 2926 (w), 2871 (w), 1620 (m), 1584 (m), 1508 (m), 1487 (m), 1466 (m), 1430 (w), 1415 (m), 1360 (w), 1350 (w), 1317 (w), 1291 (m), 1248 (s), 1211 (w), 1152 (w), 1080 (m), 1059 (s), 1045 (w), 935 (m), 861 (m), 825 (m), 782 (m), 758 (m), 702 (m), 702 (m), 675 (m) cm^{-1}. Elemental analysis (%) calculated for $C_{11}H_{12}N_2O_2$ (204.2): C 64.69, H 5.92, N 13.72; found: C 64.71, H 6.05, N 13.73. Single crystals were obtained upon slow cooling of a saturated solution in light petroleum. The solid-state structure of H_2L was determined by X-ray diffraction.

*Synthesis of $[Mn_2^{III}Ni_3^{II}L_4(LH)_2Cl_2(H_2O)_2]$ (**1**).* A solution of NEt_3 (23 mg, 0.22 mmol, 1.5 equiv) in acetonitrile (3 mL) was added dropwise to a solution of $NiCl_2\cdot 6H_2O$ (26 mg, 0.110 mmol, 0.75 equiv) and H_2L (30 mg, 0.147 mmol, 1 equiv) in acetonitrile (15 mL) at room temperature. The resultant green solution was then added dropwise to a brown solution of $MnCl_2\cdot 4H_2O$ (29 mg, 0.147 mmol, 1 equiv), H_2L (30 mg, 0.147 mmol, 1 equiv), and NEt_3 (23 mg, 0.22 mmol, 1.5 equiv) in acetonitrile (15 mL), and the reaction mixture was stirred for 8 h at room temperature. Evaporation of all volatile material under reduced pressure gave a brown solid. This crude product was dissolved in dichloromethane (25 mL), and plate-shaped brown crystals of $\mathbf{1}\cdot 8CH_2Cl_2$ were obtained by slow evaporation of the solution. Due to the loss of solvent molecules the crystals crumble after separation from the mother liquor. Yield: 40 mg (48%). IR (KBr): $\tilde{\nu}$ 3582 (w), 3458 (br), 3131 (w), 3111 (w), 3052 (w), 2928 (m), 2841 (m), 1627 (m), 1598 (s), 1563 (m), 1502 (w), 1506 (s), 1470 (s), 1443 (s), 1412 (m), 1357 (w), 1308 (s), 1256 (w), 1234 (w), 1204 (w), 1132 (s), 1084 (s), 948 (w), 857 (m), 850 (w), 805 (w), 766 (m), 743 (w), 701 (m), 642 (w), 609 (m) cm^{-1}. Elemental analysis (%) calculated for $C_{67.5}H_{69}N_{12}O_{14}Mn_2Ni_3Cl_5$ ($\mathbf{1}\cdot 1.5CH_2Cl_2$; 1735.6): C 46.71, H 4.01, N 9.68; found: C 46.46, H 4.18, N 9.67. Most of the lattice solvent molecules are lost upon drying the crystalline material.

*Synthesis of $[Mn_2^{III}Ni_3^{II}L_4(LH)_2Br_2(H_2O)_2]$ (**2**).* Compound **2** was obtained in a similar manner as described for **1**, but using $MnBr_2\cdot 4H_2O$ instead of $MnCl_2\cdot 4H_2O$. Brown crystals of $\mathbf{2}\cdot 8CH_2Cl_2$ were obtained by slow evaporation of a solution of the crude product in dichlormethane. Yield: 50 mg (54%). IR (KBr): $\tilde{\nu}$ 3588 (w), 3437 (br), 3113 (w), 3052 (w), 2928 (m), 2842 (m), 2363 (w), 1629 (w), 1598 (s), 1561 (m), 1507 (s), 1469 (s), 1443 (s), 1412 (m), 1361 (m), 1325 (w), 1306 (s), 1269 (w), 1256 (w), 1233 (w), 1202 (w), 1156 (w), 1134 (s), 1084 (s), 1050 (w), 948 (w), 856 (m), 841 (w), 769 (w), 756 (m), 742 (w), 700 (m), 664 (w), 635 (w), 638 (w), 610 (m) cm^{-1}. Elemental analysis (%) calculated for $C_{67.5}H_{69}N_{12}O_{14}Mn_2Ni_3Cl_3Br_2$ (1731.5): C 44.44, H 3.81, N 9.21; found: C 44.29, H 4.16, N 9.15.

Physical Measurements. Melting points were determined with a SRS (Stanford Research Systems) Opti Melt apparatus using open capillaries; the values are uncorrected. Elemental analyses were performed by the analytical laboratory of the Institute of Inorganic Chemistry at Georg-August-Universität Göttingen using an Elementar Vario EL III. NMR measurements were performed, unless indicated otherwise, at 25 °C on Bruker Avance 200, 300, and 500 spectrometers. ^1H and ^{13}C chemical shifts were calibrated internally to the solvent signals (7.24 and 77.0 ppm for $CDCl_3$). EI-MS-spectra were recorded on a Finnigan MAT 95. Values for *m*/*z* are given for the most intense peak of the isotope envelope. IR spectra were recorded on a Digilab Excalibur series FTS 3000 spectrometer. Variable-temperature, solid-state direct current (dc) and alternating current (ac) magnetic susceptibility data down to 1.8 K were collected on a Quantum Design MPMS-5S SQUID magnetometer equipped with a 5 T dc magnet (for these measurements the powdered samples were contained in a gel bucket and fixed in a nonmagnetic sample holder). Diamagnetic corrections were applied to the observed paramagnetic susceptibilities using Pascal's constants. Magnetic studies below 1.8 K were carried out on single crystals, using a homemade micro-Hall-bar magnetometer equipped with several 10 × 10 μm^2 Hall bars. Micrometer-sized single crystals of the sample were placed on top of the active area of the Hall bars. The crystals were oriented with the easy axis approximately parallel to the applied magnetic field. High-field/high-frequency electron spin resonance

(HF-ESR) studies in a frequency range 50−400 GHz in magnetic fields up to 15 T were performed using a homemade spectrometer based on a Millimeter Wave Vector Network Analyzer (AB Millimetré).[46]

X-ray Crystallography. Crystal data and details of the data collections are given in Table S1 (Supporting Material). X-ray data were collected on a STOE IPDS II diffractometer (graphite monochromated Mo Kα radiation, $\lambda = 0.71073$ Å) by use of ω scans at −140 °C. The structures were solved by direct methods and refined on F^2 using all reflections with SHELX-97.[47] All non-hydrogen atoms were refined anisotropically. Most hydrogen atoms were placed in calculated positions and assigned to an isotropic displacement parameter of 0.08 Å^2. In the case of the oxygen-bound hydrogen atoms H4 and H7A/B in **2**·8CH$_2$Cl$_2$ DFIX restraints (d_{O-H} = 0.82 Å) were applied. Those hydrogen atoms could not be located in **1**·8CH$_2$Cl$_2$. No restraints or constraints were used for the oxygen-bound hydrogen atoms in H$_2$L. The correct absolute structure of H$_2$L could not be determined. Face-indexed absorption corrections for all compounds were performed numerically with the program X-RED.[48]

■ ASSOCIATED CONTENT

Ⓢ Supporting Information. CIF files; plots of the molecular structures of **1**·8CH$_2$Cl$_2$, **2**·8CH$_2$Cl$_2$ and H$_2$L with atom distances and bond angles and crystal data. This material is available free of charge via the Internet at http://pubs.acs.org.

■ AUTHOR INFORMATION

Corresponding Author

V.Kataev@ifw-dresden.de; phm@physik.uni-erlangen.de; franc.meyer@chemie.uni-goettingen.de

■ ACKNOWLEDGMENT

Financial support by the DFG (FM: SFB 602 “Complex Structures in Condensed Matter”; Y.K., R.K., V.K. and B.B.: FOR 1154 “Towards Molecular Spintronics”) is gratefully acknowledged.

■ REFERENCES

(1) (a) Christou, G.; Gatteschi, D.; Hendrickson, D. N.; Sessoli, R. *MRS Bull.* **2000**, *25*, 66–71. (b) Chudnovsky, E. M. *Science* **1996**, *274*, 938–939. (c) Gatteschi, D.; Sessoli, R. *Angew. Chem.* **2003**, *115*, 278–309.

(2) (a) Affronte, M. J. *Mater. Chem.* **2009**, *19*, 1731–1737. (b) Ardavan, A.; Blundell, S. J. *J. Mater. Chem.* **2009**, *19*, 1754–1760. (c) Lehmann, J.; Gaita-Ariño, A.; Coronado, E.; Loss, D. *J. Mater. Chem.* **2009**, *19*, 1672–1677. (d) Camarero, J.; Coronado, E. *J. Mater. Chem.* **2009**, *19*, 1687–1684. (e) Bogani, L.; Wernsdorfer, W. *Nat. Mater.* **2008**, *7*, 179–186.

(3) (a) Sessoli, R.; Gatteschi, D.; Caneschi, A.; Novak, M. A. *Nature* **1993**, *365*, 141–143. (b) Sessoli, R.; Tsai, H. L.; Schake, A. R.; Wang, S. Y.; Vincent, J. B.; Folting, K.; Gatteschi, D.; Christou, G.; Hendrickson, D. N. *J. Am. Chem. Soc.* **1993**, *115*, 1804–1816.

(4) Bagai, R.; Christou, G. *Chem. Soc. Rev.* **2009**, *38*, 1011–1026.

(5) (a) Miyasaka, H.; Clérac, R.; Wernsdorfer, W.; Lecren, L.; Bonhomme, C.; Sugiura, K.-I.; Yamashita, M. *Angew. Chem.* **2004**, *116*, 2861–2865. (b) Sanudo, E. C.; Wernsdorfer, W.; Abboud, K. A.; Christou, G. *Inorg. Chem.* **2004**, *43*, 4137–4144. (c) Taguchi, T.; Wernsdorfer, W.; Abboud, K. A.; Christou, G. *Inorg. Chem.* **2010**, *49*, 199–208.

(6) Sun, Z.; Grant, C. M.; Castro, S. L.; Hendrickson, D. N.; Christou, G. *Chem. Commun.* **1998**, 721–722.

(7) (a) Gatteschi, D.; Sessoli, R.; Cornia, A. *Chem. Commun.* **2000**, 725–732. (b) Accorsi, S.; Barra, A.-L.; Caneschi, A.; Chastanet, G.; Cornia, A.; Fabretti, A. C.; Gatteschi, D.; Mortalo, C.; Olivieri, E.; Parenti, F.; Rosa, P.; Sessoli, R.; Sorace, L.; Wernsdorfer, W.; Zobbi, L. *J. Am. Chem. Soc.* **2006**, *128*, 4742–4755. (c) Boudalis, A. K.; Sanakis, Y.; Clemente-Juan, J. M.; Donnadieu, B.; Nastopoulos, V.; Mari, A.; Coppel, Y.; Tuchagues, J.-P.; Perlepes, S. P. *Chem.—Eur. J.* **2008**, *14*, 2514–2526. (d) Ako, A. M.; Mereacre, V.; Lan, Y.; Wernsdorfer, W.; Clérac, R.; Anson, C. E.; Powell, A. K. *Inorg. Chem.* **2010**, *49*, 1–3.

(8) (a) Moubaraki, B.; Murray, K. S.; Hudson, T. A.; Robson, R. *Eur. J. Inorg. Chem.* **2008**, 4525–4529. (b) Murray, K. S. *Aust. J. Chem.* **2009**, *62*, 1081–1101. (c) Murrie, M. *Chem. Soc. Rev.* **2010**, *39*, 1986–1995.

(9) (a) Andres, H.; Basler, R.; Blake, A. J.; Cadiou, C.; Chaboussant, G.; Grant, C. M.; Güdel, H.-U.; Murrie, M.; Parsons, S.; Paulsen, C.; Semadini, F.; Villar, V.; Wernsdorfer, W.; Winpenny, R. E. P. *Chem.—Eur. J.* **2002**, *8*, 4867–4876. (b) Ochsenbein, S. T.; Murrie, M.; Rusanow, E.; Stoeckli-Evans, H.; Sekine, C.; Güdel, H.-U. *Inorg. Chem.* **2002**, *41*, 5133–5140. (c) Bell, A.; Aromi, G.; Teat, S. J.; Wernsdorfer, W.; Winpenny, R. E. P. *Chem. Commun.* **2005**, 2808–2810. (d) Aromi, G.; Parsons, S.; Wernsdorfer, W.; Brechin, E. K.; McInnes, E. J. L. *Chem. Commun.* **2005**, 5038–5040.

(10) Milios, C. J.; Vinslava, A.; Wernsdorfer, W.; Moggach, S.; Parsons, S.; Perlepes, S. P.; Christou, G.; Brechin, E. K. *J. Am. Chem. Soc.* **2007**, *129*, 2754–2755.

(11) (a) Cremades, E.; Cano, J.; Ruiz, E.; Rajaraman, G.; Milios, C. J.; Brechin, E. K. *Inorg. Chem.* **2009**, *48*, 8012–8019. (b) Inglis, R.; Jones, L. F.; Milios, C. J.; Datta, S.; Collins, A.; Parsons, S.; Wernsdorfer, W.; Hill, S.; Perlepes, S. P.; Piligkos, S.; Brechin, E. K. *Dalton Trans.* **2009**, 3403–3412.

(12) Gatteschi, D.; Sessolis, R.; Villain, J. *Molecular Nanomagnets*; Oxford University Press: New York, 2006.

(13) Cirera, J.; Ruiz, E.; Alvarez, S.; Neese, F.; Kortus, J. *Chem.—Eur. J.* **2009**, *15*, 4078–4087.

(14) Oshio, H.; Nakano, M. *Chem.—Eur. J.* **2005**, *11*, 5178–5185.

(15) Waldmann, O. *Inorg. Chem.* **2007**, *46*, 10035–10037.

(16) Ruiz, E.; Cirera, J.; Cano, J.; Alvarez, S.; Loose, C.; Kortus, J. *Chem. Commun.* **2008**, 52–54.

(17) Hill, S.; Datta, S.; Liu, J.; Inglis, R.; Milios, C. J.; Feng, P. L.; Henderson, J. J.; del Barco, E.; Brechin, E. K.; Hendrickson, D. N. *Dalton Trans.* **2010**, *39*, 4693–4707.

(18) Wernsdorfer, W.; Aliaga Alcalde, N.; Hendrickson, D. N.; Christou, G. *Nature* **2002**, *416*, 406–409.

(19) (a) Hill, S.; Edwards, R. S.; Aliaga-Alcade, N.; Christou, G. *Science* **2003**, *302*, 1015–1018. (b) Tiron, R.; Wernsdorfer, W.; Foguet-Albiol, D.; Aliaga-Alcade, N.; Christou, G. *Phys. Rev. Lett.* **2003**, *91* (227203), 1–4.

(20) (a) Yamaguchi, A.; Kusumi, N.; Ishimoto, H.; Mitamura, H.; Goto, T.; Mori, N.; Nakano, M.; Awaga, K.; Yoo, J.; Hendrickson, D. N.; Christou, G. *J. Phys. Soc. Jpn.* **2002**, *71*, 414–417. (b) Affronte, M.; Lasjaunias, J. C.; Wernsdorfer, W.; Sessoli, R.; Gatteschi, D.; Heath, S. L.; Fort, A.; Rettori, A. *Phys. Rev. B* **2002**, *66*, 064408/1–064408/7. (c) Asada, H.; Ozeki, M.; Fujiwara, M.; Matsushita, T. *Chem. Lett.* **1999**, 525–526. (d) Dey, M.; Rao, C. P.; Saarenketo, P. K.; Rissanen, K. *Inorg. Chem. Commun.* **2002**, *5*, 924–928. (e) Wittick, L. M.; Murray, K. S.; Moubaraki, B.; Batten, S. R.; Spiccia, L.; Berry, K. J. *Dalton Trans.* **2004**, 1003–1011.

(21) Boskovic, C.; Bircher, R.; Tregenna-Piggott, W. L. P.; Güdel, U. H.; Paulsen, C.; Wernsdorfer, W.; Baara, -L. A.; Khatsko, E.; Neels, A.; Stoeckli-Evans, H. *J. Am. Chem. Soc.* **2003**, *125*, 14046–14058.

(22) Miyasaka, H.; Yamashita, M. *Dalton Trans.* **2007**, 399–406.

(23) Oshio, H.; Nihei, M.; Yoshida, A.; Nojiri, H.; Nakano, M.; Yamaguchi, A.; Karaki, Y.; Ishimoto, H. *Chem.—Eur. J.* **2005**, *11*, 843–848.

(24) Oshio, H.; Nihei, M.; Koizumi, S.; Shiga, T.; Nojiri, H.; Nakano, M.; Shirakawa, N.; Akatsu, M. *J. Am. Chem. Soc.* **2005**, *127*, 4568–4569.

(25) Kachi-Terajima, C.; Miyasaka, H.; Saitoh, A.; Shirakawa, N.; Yamashita, M.; Clérac, R. *Inorg. Chem.* **2007**, *46*, 5861–5872.

(26) Li, D.; Parkin, S.; Wang, G.; Yee, T. G.; Cle’ rac, R.; Wernsdorfer, W.; Holmes, M. S. *J. Am. Chem. Soc.* **2006**, *128*, 4214–4215.

(27) Glaser, T.; Heidemeier, M.; Weyhermüller, T.; Hoffmann, R.-D.; Rupp, H.; Müller, P. *Angew. Chem., Int. Ed.* **2006**, *45*, 6033–6037.

(28) (a) Feng, L. P.; Beedle, C. C.; Wernsdorfer, W.; Koo, C.; Nakano, M.; Hill, S.; Hendrickson, N. D. *Inorg. Chem.* **2007**, *46*, 8126–8128. (b) Feng, L. P.; Beedle, C. C.; Koo, C.; Wernsdorfer, W.; Nakano, M.; Hill, S.; Hendrickson, N. D. *Inorg. Chem.* **2008**, *47*, 3188–3204.

(29) Glaser, T.; Heidemeier, M.; Krickemeyer, E.; Bögge, H.; Stammler, A.; Fröhlich, R.; Bill, E.; Schnack, J. *Inorg. Chem.* **2007**, *48*, 607–620.

(30) (a) Winpenny, R. E. P. *Dalton Trans.* **2002**, 1–10. (b) Aromi, G.; Brechin, E. K. *Struct. Bonding (Berlin)* **2006**, *122*, 1–67.

(31) Tasiopoulos, A. J.; Perlepes, S. P. *Dalton Trans.* **2008**, 5537–5555.

(32) (a) Tanase, S.; Aromi, G.; Bouwman, E.; Kooijman, H.; Spek, A. L.; Reedijk, J. *Chem. Commun.* **2005**, 3147. (b) Viciano-Chumillas, M.; Tanase, S.; Aromi, G.; Smits, J. M. M.; de Gelder, R.; Solans, X.; Bouwman, E.; Reedijk, J. *Eur. J. Inorg. Chem.* **2007**, 2635–2640. (c) Viciano-Chumillas, M.; de Ruiter, G.; Tanase, S.; Smits, J. M. M.; de Gelder, R.; Mutikainen, I.; Turpeinen, U.; de Jongh, L. J.; Reedijk, J. *Dalton Trans.* **2010**, *39*, 4991–4998.

(33) (a) Klingele, J.; Dechert, S.; Meyer, F. *Coord. Chem. Rev.* **2009**, *253*, 2698–2741. (b) Chaudhuri, P.; Kataev, V.; Büchner, B.; Klauss, H.-H.; Kersting, B.; Meyer, F. *Coord. Chem. Rev.* **2009**, *253*, 2261–2285.

(34) Pleier, A.-K; Glas, H; Grosche, M.; Sirsch, P.; Thiel, W. R. *Synthesis* **2001**, 55–62.

(35) Liu, W.; Thorp, H. H. *Inorg. Chem.* **1993**, *32*, 4102–4105.

(36) Although hydrogen atoms could not be located in the crystallographic analysis of **1**·8CH$_2$Cl$_2$, an H-bonding pattern similar to the situation in **2**·8CH$_2$Cl$_2$ is likely.

(37) Geim, A. K.; Dubonos, S. V.; Lok, J. G. S.; Grigorieva, I. V.; Maan, J. C.; Hansen, L. T.; Lindelof, P. E. *Appl. Phys. Lett.* **1997**, *71*, 2379–2381.

(38) Abragam, A.; Bleaney, B. *Electron Paramagnetic Resonance of Transition Ions*; Oxford University Press: London, 1970.

(39) Gatteschi, D.; Sessoli, R.; Villain, J. *Molecular Nanomagnets*; Oxford University Press: Oxford, 2006.

(40) Bencini, A.; Gatteschi, D. *EPR of Exchange Coupled Systems*; Springer: New York, 1990.

(41) Stoll, S.; Schweiger, A. *J. Magn. Reson.* **2006**, *178*, 42–55.

(42) Macrae, C. F.; Bruno, I. J.; Chisholm, J. A.; Edgington, P. R.; McCabe, P.; Pidcock, E.; Rodriguez-Monge, L.; Taylor, R.; van de Streek, J.; Wood, P. A. *J. Appl. Crystallogr.* **2008**, *41*, 466–470.

(43) Spek, A. L. *J. Appl. Crystallogr.* **2003**, *36*, 7–13.

(44) Janiak, C. *J. Chem. Soc., Dalton Trans.* **2000**, 3885–3896.

(45) For 1D assembly of homometallic Mn^{III} SMMs, see for example: (a) Lecren, L.; Roubeau, O.; Coulon, C.; Li., Y.-G.; Le Goff, X. F.; Wernsdorfer, W.; Miyasaka, H.; Clérac, R. *J. Am. Chem. Soc.* **2005**, *127*, 17353–17363. (b) Jeon, I.-R.; Ababei, R.; Lecren, L.; Li, Y.-G.; Wernsdorfer, W.; Roubeau, O.; Mathonière, C.; Clérac, R. *Dalton Trans.* **2010**, *39*, 4744–4746. (c) Haryono, M.; Kalisz, M.; Sibille, R.; Lescouëzec, R.; Fave, C.; Trippe-Allard, G.; Li, Y.; Seuleiman, M.; Rousselière, H.; Balkhy, A. M.; Lacroix, J.-C.; Journaux, Y. *Dalton Trans.* **2010**, *39*, 4751–4756.

(46) Golze, C.; Alfonsov, A.; Klingeler, R.; Büchner, B.; Kataev, V.; Mennerich, C.; Klauss, H.-H.; Goiran, M.; Broto, J.-M.; Rakoto, H.; Demeshko, S.; Leibeling, G.; Meyer, F. *Phys. Rev. B* **2006**, *73*, 224403/1–224403/8.

(47) Sheldrick, G. M. *Acta Crystallogr.* **2008**, *A64*, 112–122.

(48) *X-RED*; Stoe & Cie GmbH: Darmstadt, Germany, 2002.